NJC

ROYAL SOCIETY OF CHEMISTRY

PAPER

View Article Online
View Journal | View Issue

Cite this: *New J. Chem.*, 2025, **49**, 13164

Third-order nonlinear optical properties of π-stacked donor–acceptor cyclophanes: a DFT investigation†

Yu Yang, Yan Yan and Na Hou*

The electronic and nonlinear optical (NLO) properties of cyclophane-based complexes were modulated by introducing various donor groups and acceptor groups. The donor groups comprise carbazole (KZ), benzo[1,2-*b*:4,5-*b*′]dithiophene (BDT), and dihydroindolo[3,2-*b*]indole (DN), while the acceptor groups comprise 1,4,5,8-naphthalenetetracarboxylic diimide (NDI) and 4,4-difluoro-4-bora-3*a*,4*a*-diaza-*s*-indacene (BOD). Reduced density gradient analysis confirmed the characteristic weak π–π stacking interactions between the donor and acceptor units. Significantly, these complexes exhibit remarkably large second hyperpolarizabilities of 3.43×10^5–5.62×10^5 a.u., with NDI-based systems showing consistently superior NLO responses compared to their BOD-based counterparts. A comprehensive analysis of electronic transitions, hyperpolarizability tensors, and hyperpolarizability densities provides a deep understanding of the nature of optical properties. In NDI/BOD-based systems, the excitation transitions exhibit significant charge transfer character from the donor moieties (KZ/BDT/DN) to the NDI/BOD unit, along with local excitation (LE) components. However, BOD-based systems additionally demonstrate reverse charge transfer from the BOD unit back to the KZ/BDT moieties. The decomposition of the hyperpolarizability contribution analysis reveals that stronger electron-donating groups enhance positive contributions. Notably, BOD acceptors exhibit anomalous negative effects compared to NDI analogues. This research offers a basis for understanding the structure–property relationships of cyclophanes.

Received 14th May 2025,
Accepted 4th July 2025

DOI: 10.1039/d5nj02033f

rsc.li/njc

1. Introduction

With rapid advances in nonlinear optics, nonlinear optical materials draw significant interest for their potential in image encryption, optical data storage, dynamic holography, and other advanced technologies.[1–3] Numerous organometallic, inorganic, organic, organic–inorganic hybrid materials are being explored as effective NLO materials.[4–7] Organic compounds exhibit pronounced intramolecular charge transfer (ICT), where electron density migrates through the π-conjugated bridge between donor (D) and acceptor (A) moieties—a fundamental process underlying their NLO properties.[8,9] Consequently, by strategically assembling the donor, π-spacer, and acceptor moieties, the molecular NLO response can be significantly enhanced.

Notably, small-molecule aromatic diimides—1,4,5,8-naphthalenetetracarboxylic diimide (NDI) and 3,4,9,10-perylenetetracarboxylic diimide (PDI)—are well-known as electron-deficient π-acceptors.[10] In recent years, Wang *et al.* have conducted extensive research on the assembly of naphthalene and pyromellitic diimide-based materials, analyzing the nonlinear optical properties of their triangular dimers and the organic co-crystals formed using naphthalenediimide-based triangular macrocycles with coronene.[11–13] Their findings revealed that the larger conjugated surface of PDI and the isosceles triangle assembly mode facilitated intramolecular charge transfer, thereby enhancing its NLO properties.[11] On the other hand, electron-withdrawing units such as carbazole (KZ), benzo[1,2-*b*:4,5-*b*′]dithiophene (BDT), and dihydroindolo[3,2-*b*]indole (DN) have been widely utilized in the synthesis of photoelectric materials.[14–16] Experimental and theoretical studies on the NLO properties of carbazole-coumarin-based chalcones with different donor substituents were performed.[17] In 2012, BDT was first incorporated into NLO materials, with HRS confirming its role as a promising π-electron bridge.[18]

Cyclophanes, compounds in which aromatic rings are constrained into cyclic structures by bridging bonds or molecular linkers, have emerged as active materials with properties superior to their simpler constituents.[19] As early as 2009, researchers synthesized a series of planar chiral asymmetric naphthalenediimide cyclophanes, which consist of two different

---

Key Laboratory of Magnetic Molecules and Magnetic Information Materials of Ministry of Education & School of Chemistry and Chemical Engineering of Shanxi Normal University, Taiyuan 030031, China. E-mail: 703101@sxnu.edu.cn

† Electronic supplementary information (ESI) available. See DOI: **https://doi.org/10.1039/d5nj02033f**

naphthalenediimides interconnected by rigid *meta*-dimethylenebenzene spacers.[20] Bansal *et al.* synthesized a new cofacially stacked NDI···NDI dimer with the shortest NDI···NDI contacts realized to date, enabling large electronic coupling of the monomer fragments.[21] More recently, Wang *et al.* synthesized a series of D/A cyclophanes featuring two cofacially stacked donor and acceptor moieties (see Scheme S1, ESI†).[22] The acceptor moieties (NDI/PDI) and donor moieties [carbazole (C8KZ), benzo[1,2-*b*:4,5-*b*′]dithiophene (C8BDT), and dihydroindolo[3,2-*b*]indole (C8DN)] were employed in their studies. Due to the intramolecular CT interactions between the electron donor and electron acceptor molecules, these D/A π-stacking cyclophanes are expected to exhibit nonlinear optical properties.

Inspired by the above discussions, we performed theoretical investigations of the NLO properties of a series of cyclophanes to enrich the research on π-stacking cyclophanes. As shown in Fig. 1, the studied compounds include **KZ-NDI**, **BDT-NDI**, **DN-NDI**, **KZ-BOD**, **BDT-BOD**, and **DN-BOD**. BODIPY (4,4-difluoro-4-bora-3*a*,4*a*-diaza-*s*-indacene, boron dipyrromethene, BOD) exhibits properties that can be tuned *via* core modifications, drawing considerable research interest.[23–25] Several BODIPY-based donor–acceptor systems have been reported as promising NLO materials.[26–29] Thus, BODIPY was selected as the electron acceptor in three cyclophane systems: **KZ-BOD**, **BDT-BOD**, and **DN-BOD**. The objective of this work is to provide a theoretical foundation and novel design concepts for the development of innovative NLO materials.

2. Computational details

All calculations were carried out with the Gaussian 09 package.[30] Wave function analyses were performed using the Multiwfn 3.8 (dev) code,[31] and the isosurface maps were visualized using the VMD software.[32]

Geometry optimizations for the studied compounds were performed using the M06-2X[33] and CAM-B3LYP[34] functionals with the 6-31G(d,p) basis set, incorporating Grimme's D3 correction to account for long-range dispersion effects. This D3 scheme, an additive correction to standard Kohn–Sham DFT, implements the original zero-damping formalism. The DFT-D3 correction approach demonstrates high accuracy, reduced empirical parameterization, and broad applicability in the study of noncovalent complexes.[35,36] Vibrational frequency analyses confirmed that the optimized structures correspond to real local minima on the potential energy surface. Atomic charges were calculated by natural population analysis (NPA)[37] at the CAM-B3LYP/6-31G(d,p) level of theory. The atomic dipole moment-corrected Hirshfeld population (ADCH)[38] analysis was conducted using the Multiwfn program.

The isotropic average polarizability (α_{iso}) and second hyperpolarizability (γ_{tot}) are expressed as follows:

$$\alpha_{\text{iso}} = \frac{1}{3}\left(\alpha_{xx} + \alpha_{yy} + \alpha_{zz}\right) \quad (1)$$

$$\gamma_{\text{tot}} = \frac{1}{5}\left(\gamma_{xxxx} + \gamma_{yyyy} + \gamma_{zzzz} + 2\gamma_{xxyy} + 2\gamma_{xxzz} + 2\gamma_{yyzz}\right) \quad (2)$$

The γ density analysis was performed to evaluate the local contributions of different spatial regions to hyperpolarizability.[39] The electron density of a system $\rho(r, F)$ can be defined with respect to the external field F:

$$\rho(r,F) = \rho^{(0)}(r) + \sum_j \rho_j^{(1)}(r)F_j + \frac{1}{2!}\sum_j\sum_k \rho_{jk}^{(2)}(r)F_jF_k + \frac{1}{3!}\sum_j\sum_k\sum_l \rho_{jkl}^{(3)}(r)F_jF_kF_l\ldots \quad (3)$$

The corresponding component of γ_{yyyy} along the y-axis can be written as follows:

$$\gamma_{yyyy}^{\text{FF}} = \frac{1}{3!}\int -y\rho_{yyy}^{(3)}(r)\mathrm{d}r \quad (4)$$

where the second hyperpolarizability density is defined as follows:

$$\rho_{yyy}^{(3)}(r) = \left.\frac{\partial^3\rho(r)}{\partial {F_y}^3}\right|_{F=0} = \frac{\rho(2F_y) - 2\rho(F_y) + 2\rho(-F_y) - \rho(-2F_y)}{2(F_y)^3} \quad (5)$$

The second hyperpolarizability was evaluated using the analytical method and the finite-field-mixed method at the CAM-B3LYP/6-31+G(d) level. The hyperpolarizability density was computed using the finite-field (FF) method at the same

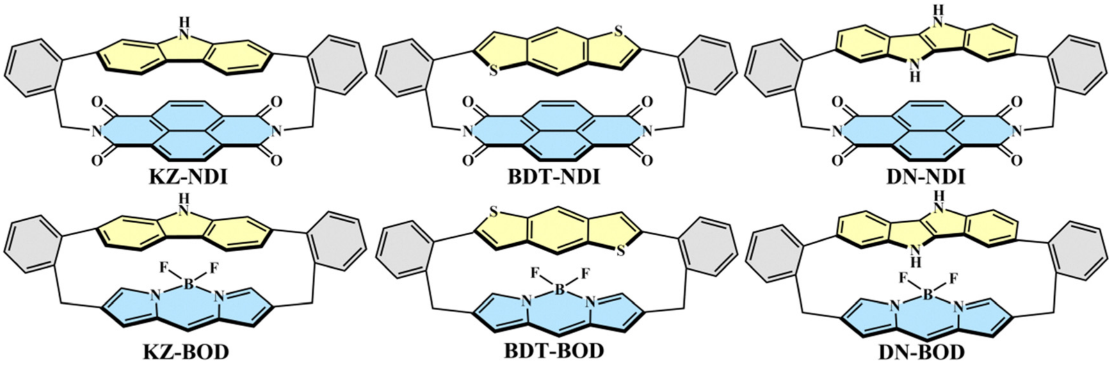

Fig. 1 Chemical structures of **KZ-NDI**, **BDT-NDI**, **DN-NDI**, **KZ-BOD**, **BDT-BOD**, and **DN-BOD**.

level. Furthermore, the UV-vis absorption spectra are simulated using time-dependent DFT (TDDFT) with the CAM-B3LYP/6-31+G(d) method, providing electronic properties such as oscillator strengths and transition energies. The solvent effects were considered in the calculations of the optical responses and electronic transition properties using the polarizable continuum model (PCM)[40] with dichloromethane as the solvent.

3. Results and discussion

3.1 Geometrical structure

The geometries of the studied complexes were optimized using the CAM-B3LYP-D3 and M06-2X-D3 functionals with the 6-31G(d,p) basis set. These macrocyclic complexes were designed by covalently connecting electron-donor (KZ/BDT/DN) and electron-acceptor (NDI/BOD) units *via* two –C_6H_4–CH_2– bridges, following the structural motif of experimentally reported D/A cyclophanes (C8KZ-NDI, C8BDT-NDI, and C8DN-NDI).[22] A one-pot synthesis of D/A cyclophanes was achieved *via* Pd(0)-catalyzed Stille coupling between NDI-BN and double tin compounds.[22] We predict that structurally analogous NDI-based systems can be synthesized using the same methodology. The BODIPY core can be modified easily to fine-tune the photonic and electronic properties.[41] A BODIPY derivative functionalized with two benzyl groups ($C_6H_5CH_2$-) at the β-positions has been synthesized.[42] We anticipate the experimental synthesis of the BOD-based compound. Fig. S1 (ESI†) displays the structures of all complexes. The selected structural parameters are shown in Tables S1 and S2 (ESI†). The results indicate nearly identical geometries for both methods. CAM-B3LYP-D3-optimized geometries were used for further analysis and property evaluations. Notably, the DN moiety in **DN-NDI** displays a bent configuration, which agrees with previously reported results.[22] Similar to the **DN-NDI** structure, the DN moiety in **DN-BOD** also exhibits a bent shape. In **KZ-BOD** and **BDT-BOD**, both BOD and KZ/BDT units show curved configurations. To elucidate the nature of non-covalent interactions, we employed reduced density gradient (RDG) analysis,[43] with the corresponding isosurfaces displayed in Fig. 2. The RDG isosurfaces visualize the strength and nature of non-covalent interactions through a color-coded scheme. Blue regions on the isosurface signify strong attractive interactions, typically associated with hydrogen bonding. Green areas indicate weak attractive forces, encompassing π–π interactions and van der Waals forces. In contrast, red regions denote strong repulsive interactions, often resulting from steric hindrance within ring structures. Notably, the presence of prominent green regions with light-brown hues between the donor and acceptor units provides clear evidence of weak π–π stacking interactions.

Charge analysis serves as an effective tool for understanding charge distribution. The NPA and ADCH charges are tabulated in Table 1. From Table 1, it can be inferred that the NDI/BOD fragments exhibit negative charges, confirming their roles as effective electron acceptors. For **BDT-NDI**, the BDT fragment has a negative NPA value, but the ACDH charge is positive. The charge of the BDT fragment of **BDT-NDI** is listed in Table S3 (ESI†). There are differences between NPA and ADCH charges, particularly in the charges of sulfur atoms. Due to sulfur's slightly higher electronegativity than carbon, its charge should be more negative than that of adjacent carbon atoms. The ADCH charges align with this expectation, while the NPA charges contradict this prediction. The KZ/BDT/DN fragments and covalent linkers (–C_6H_4–CH_2–) have positive NPA charges, showing that they have the characteristics of electron donors. Due to the spacing effect of the covalent linkers, the KZ/BDT/DN fragments exhibit small charges. The NDI fragments exhibit larger negative charges than the BOD fragments, indicating that BOD is less capable of capturing electrons compared to NDI. The analyses of the electrostatic potential (ESP) on the van der Waals (vdW) surface for the studied compounds provide an intuitive visualization of their charge distributions, as shown in Fig. 3. Red regions represent the areas of positive potential and correspond to electron-poor regions; whereas the blue color signifies the negative potential, corresponding to electron-rich regions. The critical local maxima and minima of electrostatic

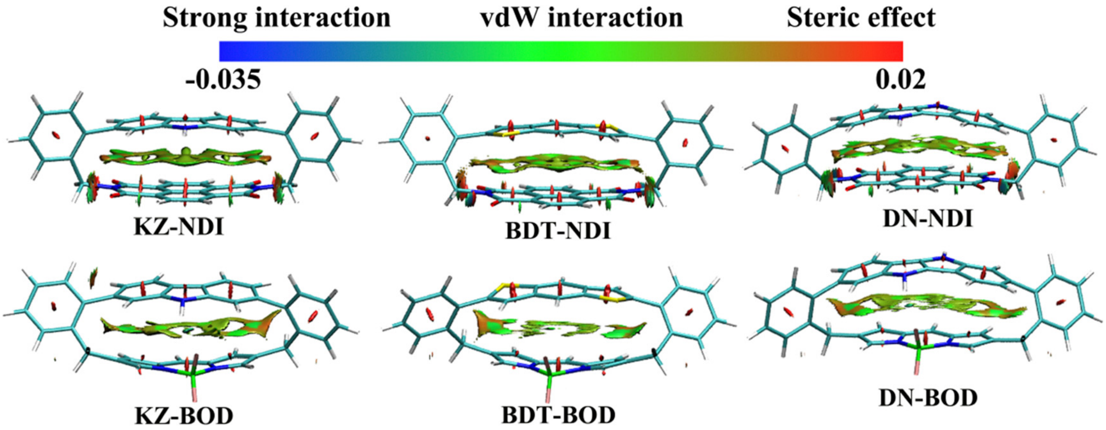

Fig. 2 Color-mapped RDG isosurface (0.50 a.u.) graphs of the complexes. The value of sign(λ_2)ρ on the surfaces is represented by filling colors according to the color bar at the top, where sign(λ_2)ρ means the sign of the second largest eigenvalue of Hessian of ρ.

Table 1 NPA and ADCH charges (|e|) of various molecular fragments

	KZ/BDT/DN fragments	$-C_6H_4-CH_2-$ (left)	$-C_6H_4-CH_2-$ (right)	NDI/BOD fragments
NPA charge				
KZ-NDI	0.001	0.250	0.250	−0.500
BDT-NDI	−0.015	0.260	0.260	−0.505
DN-NDI	0.017	0.246	0.246	−0.508
KZ-BOD	0.006	0.011	0.017	−0.034
BDT-BOD	0.019	0.021	0.023	−0.063
DN-BOD	0.029	0.008	0.012	−0.049
ADCH charge				
KZ-NDI	0.034	0.010	0.010	−0.053
BDT-NDI	0.095	0.025	0.025	−0.145
DN-NDI	0.119	0.065	0.065	−0.248
KZ-BOD	0.017	0.000	0.015	−0.031
BDT-BOD	0.001	0.013	0.027	−0.041
DN-BOD	0.044	0.014	0.045	−0.103

potential are marked by orange and cyan spheres, respectively. For **KZ/BDT/DN-NDI**, the area with evident negative ESP primarily localizes around the O=C–N–C=O groups. The most negative ESP values on the surface are −32.35, −31.75, and −34.85 kcal mol^{-1} for **KZ-NDI**, **BDT-NDI**, and **DN-NDI**, respectively. The ESP exhibits predominantly positive values across the KZ/BDT/DN moiety surface. The maximum ESP values for **KZ-NDI** and **DN-NDI** can reach as high as 48.09 and 47.58 kcal mol^{-1}, respectively. For **BDT-NDI**, the region of positive ESP (19.26 and 19.27 kcal mol^{-1}) localizes near the hydrogen atoms of the central benzene ring in the BOD moiety. This analytical finding demonstrates consistency with the ADCH charge analysis. For BOD-based complexes, the global minimum of ESP on the molecular surface localizes near the $-BF_2$ moiety, attributed to the highest electronegativity of fluorine atoms which induces greater electron density distribution. The global maximum ESP values for **KZ-BOD** and **DN-BOD** are 26.40 and 48.49 kcal mol^{-1}, respectively. For the **BDT-NDI** system, although the BDT moiety exhibits both positive and negative electrostatic potential values, the positive values (18.87 and 18.92 kcal mol^{-1}) are more pronounced.

3.2 Frontier molecular orbital properties

The distribution pattern of the highest occupied molecular orbital (HOMO) and the lowest unoccupied molecular orbital (LUMO) plays a significant role in determining the third-order NLO properties of a material. The sketches of the HOMO and LUMO, along with the energy difference (ΔE_{gap}) between the HOMO and LUMO, are shown in Fig. 4. For **KZ-NDI**, **BDT-NDI**, and **DN-NDI**, the electron density of the HOMO is mainly distributed on the KZ/BDT/DN unit, while the electron density of the LUMO is completely localized on the NDI fragment, suggesting the ICT from the donor to the acceptor part. The LUMO energies of **KZ-NDI**, **BDT-NDI**, and **DN-NDI** are very close (−2.11 to −2.13 eV), while the HOMO levels increase sequentially: **KZ-NDI** < **BDT-NDI** < **DN-NDI**. As a result, the ΔE_{gap} value decreases gradually in the order of 4.93 eV (**KZ-NDI**) > 4.76 eV (**BDT-NDI**) > 4.17 eV (**DN-NDI**). For **KZ-BOD** and **BDT-BOD**, the electron density of the LUMO delocalizes on the BOD unit, while the HOMO is localized on both the KZ/BDT and BOD units. This indicates the presence of both local excitation (LE) within the BOD and ICT from the KZ/BDT to BOD unit. For **DN-BOD**, the distribution characteristics of the frontier molecular orbitals are similar to those of **DN-NDI**. The calculated ΔE_{gap} values for **KZ-BOD** and **BDT-BOD** are 4.91 and 5.05 eV, respectively, which are larger than that of **DN-BOD** (4.47 eV). These results demonstrate that the electronic structure of cyclophanes is highly sensitive to the choice of donor and acceptor moieties. Notably, complexes containing stronger electron-donating or -accepting groups exhibit reduced energy gaps. Generally, the smaller the energy gap, the stronger the NLO response. Therefore, we can predict that NDI-based systems exhibit relatively larger NLO responses.

3.3 Absorption spectra

To understand the mechanism of charge transfer and the origin of the NLO properties, the UV-vis absorption spectra of the studied complexes were simulated using the TDDFT approach. Fig. 5 presents the computed UV-vis spectra alongside electron density difference maps (EDDM) for the key electronic transitions.

Essential electronic transition characteristics, including excitation energies, oscillator strengths, and orbital contributions for the dominant excited states as calculated by TD-CAM-B3LYP, are presented in Table 2. The relevant molecular orbitals of all systems are visualized in Fig. 6. The absorption spectrum of **KZ-NDI** displays a weak absorption at 357 nm, which originates from the HOMO−2 → LUMO transition, suggesting the charge transfer (CT) from the entire molecular framework to the acceptor (NDI) unit. Additionally, the spectrum exhibits two stronger absorption features at 242 nm and 220 nm, where the higher-wavelength band (242 nm) represents a combination of CT from the KZ subunit to the NDI acceptor and LE within the KZ moiety (HOMO → LUMO+3), while the lower-wavelength feature (220 nm) corresponds to CT from the KZ unit to the entire molecular framework (HOMO → LUMO+5, HOMO → LUMO+15). The absorption spectrum of **BDT-NDI** displays a low-energy electronic transition at 356 nm, which originates from the HOMO−2 → LUMO and HOMO−4 → LUMO transitions, indicating CT from the entire molecular framework to the NDI unit. A high-energy electronic transition at 305 nm arises from the HOMO → LUMO+1 transition. This transition exhibits dual character, featuring both CT from the BDT donor to the NDI acceptor and LE within the BDT moiety. In addition, **BDT-NDI** exhibits a strong absorption at 270 nm, which arises from three distinct electronic transitions, HOMO → LUMO+2, HOMO−5 → LUMO, and HOMO−1 → LUMO+1. The HOMO−5 → LUMO transition primarily involves CT from two terminal benzene rings to the NDI unit. The HOMO → LUMO+2 and HOMO−1 → LUMO+1 transitions exhibit mixed character, showing CT from the BDT donor to the NDI acceptor alongside LE within the BDT moiety. The absorption spectrum of **DN-NDI** has three absorption peaks. A low-energy electronic transition observed at 350 nm, corresponding to HOMO−5 → LUMO and HOMO−3 → LUMO excitations, is characterized by CT from the extended molecular framework to the NDI acceptor unit. The transition at 312 nm arises from the HOMO → LUMO+3,

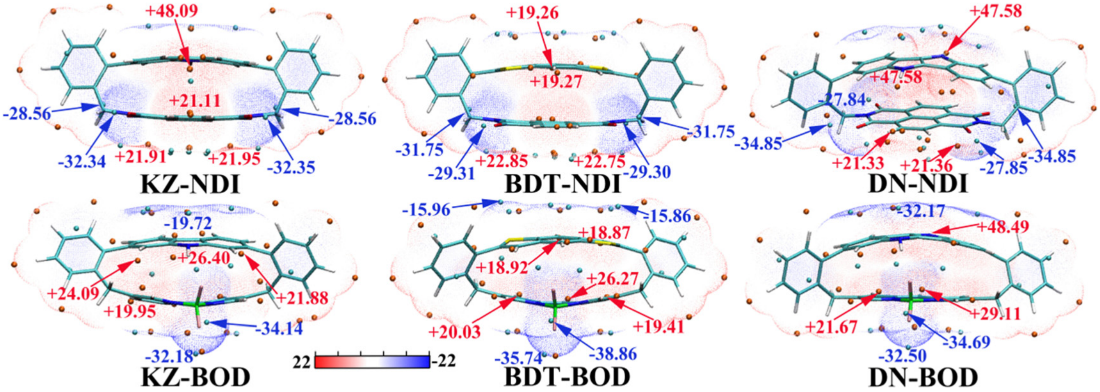

Fig. 3 Electrostatic potential (ESP) maps for all compounds. Significant surface minima and maxima of ESP are represented as cyan and orange spheres, and labeled by blue and red texts, respectively. The unit is in kcal mol^{-1}.

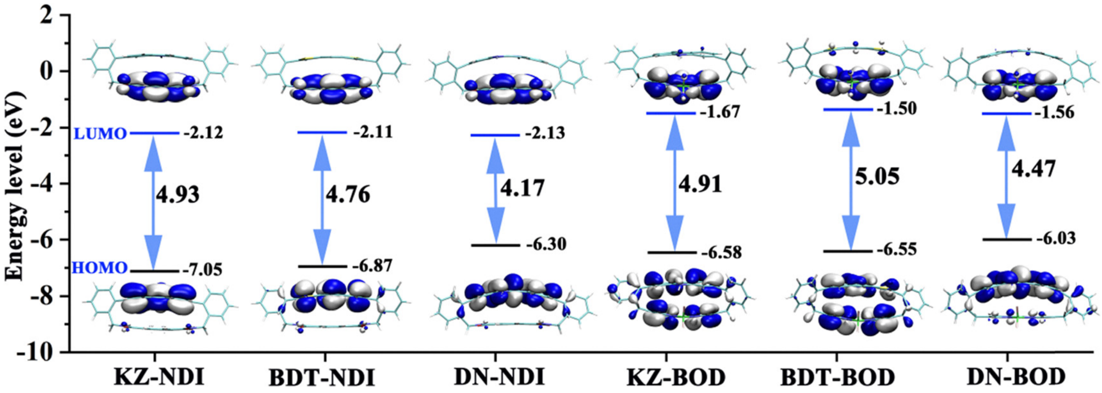

Fig. 4 Frontier molecular orbital energy levels and molecular orbital diagrams of the studied complexes.

HOMO → LUMO+2, and HOMO−9 → LUMO excitations. The HOMO → LUMO+3 and HOMO → LUMO+2 electronic transitions are attributed to ICT from the DN to the central benzene ring of the NDI moiety and LE within the DN unit. The HOMO−9 → LUMO transition predominantly arises from LE character within the NDI subunit, with minimal charge transfer contribution. The

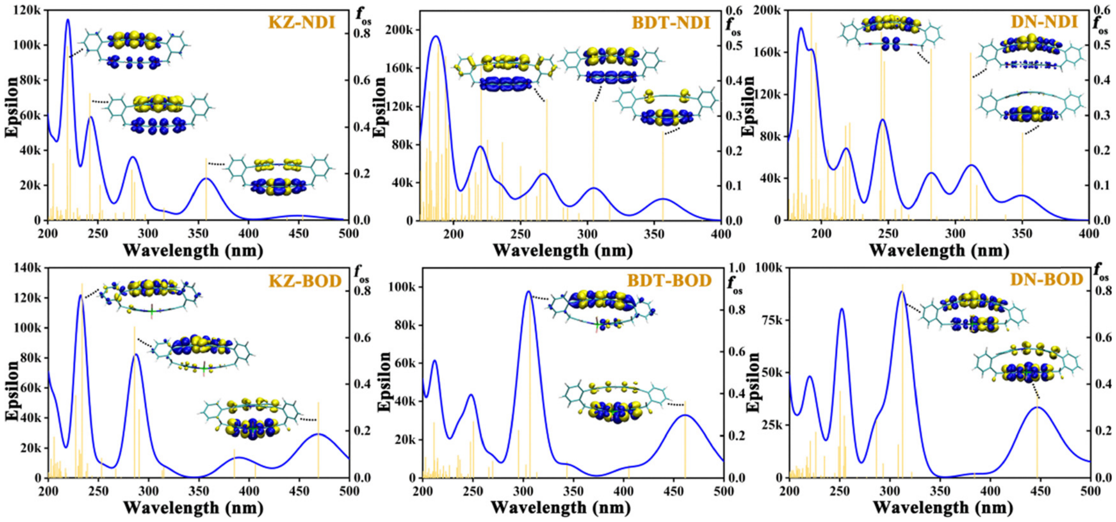

Fig. 5 The absorption spectra along with electron density difference maps (EDDMs) corresponding to the most intense electronic transitions. Blue and yellow represent an increase and a decrease in electron density, respectively.

Table 2 Simulated wavelengths (λ, nm), transition energies (ΔE_{ge}, eV), oscillator strengths (f_{os}), and major contribution for the studied complexes (H = HOMO and L = LUMO)

Complex	State	λ	ΔE_{ge}	f_{os}	$f_{os}^2/\Delta E_{ge}^5$	Major contribution
KZ-NDI	S3	357	3.47	0.265	2083	H−2 → L (81%)
	S23	242	5.12	0.543	1250	H → L+3 (63%)
	S32	220	5.64	0.744	1447	H → L+5 (38%), H → L+15 (10%)
BDT-NDI	S3	356	3.48	0.256	1916	H−2 → L (83%), H−4 → L (10%)
	S5	305	4.07	0.339	1535	H → L+1 (79%)
	S12	270	4.60	0.348	877	H → L+2 (43%), H−5 → L (17)%, H−1 → L+ 1 (13%)
DN-NDI	S3	350	3.54	0.250	1677	H−5 → L (47%), H−3 → L (44%)
	S7	312	3.98	0.478	3413	H → L+2 (70%), H → L+3 (11%), H−9 → L (11%)
	S14	282	4.40	0.489	2163	H−1 → L+2 (42%), H → L+3 (24%), H−1 → L+3 (15%)
KZ-BOD	S1	470	2.64	0.321	11 988	H → L (89%)
	S7	286	4.33	0.646	4091	H → L+1 (39%), H−1 → L+1 (34%)
	S16	234	5.30	0.831	2464	H−1 → L+2 (22%), H → L+2 (17%)
BDT-BOD	S1	461	2.69	0.363	13 957	H → L (55%), H−1 → L (41%)
	S5	307	4.04	0.894	11 080	H−1 → L+1 (41%), H → L+1 (40%)
DN-BOD	S2	446	2.78	0.371	12 367	H−1 → L (83%)
	S5	312	3.97	0.827	10 347	H → L+1 (59%), H−6 → L (19%)

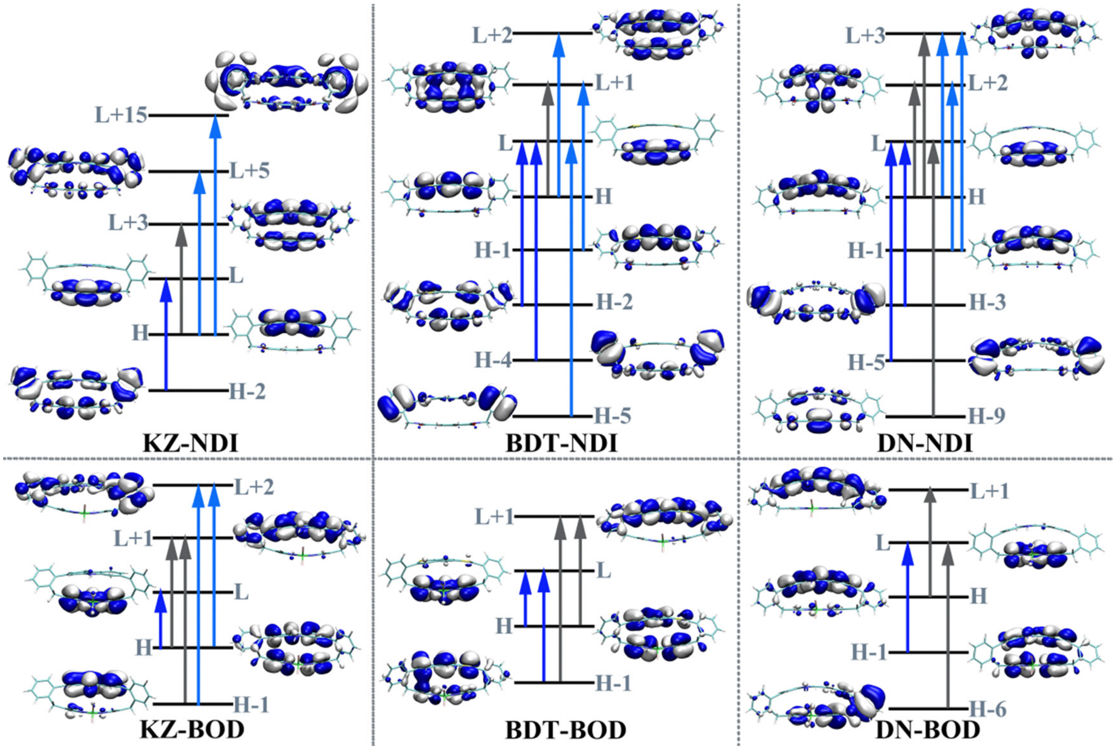

Fig. 6 Molecular orbitals involved in the crucial intense electronic transitions in the absorption spectra of complexes.

high-energy electronic transition at 282 nm arises mainly from HOMO−1 → LUMO+2, HOMO → LUMO+3, and HOMO−1 → LUMO+3, which can be viewed as the CT from the DN unit to the central benzene ring of the NDI moiety and LE of DN unit.

For **KZ-BOD**, the absorption spectrum contains one strong absorption peak at 234 nm along with two weak absorptions at 470 and 286 nm. For the electronic transition at 470 nm, HOMO → LUMO is described by the CT transition from the KZ to the BOD unit and LE within the BOD unit. The electronic transition at 286 nm is composed of HOMO → LUMO+1 and HOMO−1 → LUMO+1. Based on the analysis of HOMO and LUMO shapes, it can be viewed as LE mainly on the KZ moiety, as well as the intramolecular CT from the BOD to the KZ fragment and the neighboring bridging structure. The other absorption band at 234 nm is described by the HOMO−1 → LUMO+2 and the HOMO → LUMO+2, which can be viewed as the CT transition from the BOD to the KZ and the adjacent bridging linker, and from KZ to the benzene bridges. The **BDT-BOD** system displays two distinct electronic transitions: a high-energy transition at 307 nm arising from HOMO−1 → LUMO+1 and HOMO → LUMO+1 excitations, and a low-energy absorption peak at 461 nm arising from HOMO → LUMO and HOMO−1 → LUMO excitations. Molecular orbital analysis reveals that the 307 nm transition belongs to LE within the BDT and CT from the BOD to the BDT and the neighboring bridging structure. The 461 nm transition corresponds to the reverse CT process from BDT to BOD. Notably, **KZ-BOD** and **BDT-BOD** systems display reverse charge transfer (from the BOD unit back to the KZ/BDT moieties), a feature absent in NDI analogues. With regard to **DN-BOD**, the absorption spectrum consists of two absorption peaks at 446 and 312 nm. The low-energy transition at 446 nm is characterized by an electron transition from HOMO−1 to LUMO, indicating a combination of intermolecular CT from the DN to the BOD as well as LE within the BOD. Meanwhile, the higher-energy absorption at 312 nm arises from electron excitations involving HOMO → LUMO+1 and HOMO−6 → LUMO, which can be attributed to the LE of the DN and BOD units, along with CT from one of the benzene bridges to the BOD unit.

3.4 Linear optical properties and third-order NLO properties

It is crucial to select suitable functional and basis sets to calculate the second hyperpolarizability, which will improve the accuracy of the results.[44] The isotropic average polarizability ($\alpha_{\rm iso}$) and average second hyperpolarizability ($\gamma_{\rm tot}$) of the **DN-NDI** complex, obtained with different functionals and different Pople basis sets, are given in Table S4 (ESI†). Results obtained with the CAM-B3LYP method using the 6-31+G(d), 6-31+G(d,p), 6-311+G(d), and 6-31++G(d,p) basis sets were close to each other, but differed significantly from those calculated with 6-31G(d). Consequently, we selected the 6-31+G(d) basis set for this work due to its good balance between accuracy and the computational cost. The $\gamma_{\rm tot}$ values calculated by CAM-B3LYP, M06-2X, ωB97XD, and BH and HLYP functionals with the 6-31+G(d) basis set were nearly indistinguishable. Here, we select the CAM-B3LYP method to calculate the $\gamma_{\rm tot}$ values of all systems.

Table 3 shows $\alpha_{\rm iso}$ and $\gamma_{\rm tot}$, along with their individual components of all the studied complexes. The longitudinal tensor component α_{yy} values dominate the $\alpha_{\rm iso}$ values of all complexes, significantly exceeding the contributions of α_{xx} and α_{zz} components. These results show that the linear polarizabilities of the studied molecules are mainly determined by the electron transition along the *y*-direction. The $\alpha_{\rm iso}$ values follow distinct ascending trends: **KZ-NDI** < **BDT-NDI** < **DN-NDI** and **KZ-BOD** < **BDT-BOD** < **DN-BOD**. The polarizability is closely related to the electronic spatial extent ($\langle R^2\rangle$), a metric reflecting the electron density volume. The $\langle R^2\rangle$ values increase in the order: 23 256 a.u. (**KZ-NDI**) < 24 103 a.u. (**BDT-NDI**) < 26 991 a.u. (**DN-NDI**) and 20 118 a.u. (**KZ-BOD**) < 20 692 a.u. (**BDT-BOD**) < 23 565 a.u. (**DN-BOD**). Obviously, a larger $\langle R^2\rangle$ value corresponds to larger polarizability.

Most notably, these complexes present large static second hyperpolarizabilities, ranging from 3.43×10^5 to 5.62×10^5 a.u., which are significantly higher than that of *para*-nitroaniline (1.01×10^5 a.u.) calculated at the CAM-B3LYP/6-31+G(d) level in a dichloromethane solvent. The increasing order of the $\gamma_{\rm tot}$ amplitude is **KZ-NDI** < **BDT-NDI** < **DN-NDI** and **KZ-BOD** < **DN-BOD** < **BDT-BOD**. Crucially, NDI-based systems have significantly higher $\gamma_{\rm tot}$ values than their BOD-based counterparts, consistent with more extensive intramolecular charge transfer (ICT) in NDI systems relative to BOD systems. Higher negative charges (*e.g.*, the ADCH charge for NDI from −0.053 to −0.248 $|e|$) indicate stronger electron-withdrawing capability, enabling more extensive ICT under external fields, which is a key driver of hyperpolarizability. These findings highlight the tunability of naphthalene-derived systems for NLO responses through donor–acceptor modifications. The comparison of the $\gamma_{\rm tot}$ values between our molecules and previously reported complexes is meaningful. The cyclic trimers 2PMDI-1NDI and 2NDI-1PDI exhibit large $\gamma_{\rm tot}$ values of 4.45×10^5 a.u. and 3.68×10^5 a.u., respectively.[11] Organic co-crystals NDI-COR and NDI-2COR, assembled from naphthalenediimide-based triangular macrocycles and coronene, exhibit $\gamma_{\rm tot}$ values of 2.75×10^5 a.u. and 3.92×10^5 a.u., respectively.[12] Thus, the $\gamma_{\rm tot}$ values for the currently studied complexes are comparable to those of the reported molecules. The third-order nonlinear susceptibility value for Bn-BDY (a BODIPY dye with two C_6H_5–CH_2– substituents) in DMSO,

Table 3 The isotropic average polarizability ($\alpha_{\rm iso}$, a.u.) and second hyperpolarizability ($\gamma_{\rm tot}$, a.u.) with their individual components for the studied complexes, as well as the $\gamma_{yyyy}^{\rm FF}$ values obtained using the finite field method

	KZ-NDI	BDT-NDI	DN-NDI	KZ-BOD	BDT-BOD	DN-BOD
α_{xx}	602	589	625	479	494	518
α_{yy}	898	962	1027	990	1024	1076
α_{zz}	440	445	456	402	416	438
$\alpha_{\rm iso}$	647	665	703	623	645	678
γ_{xxxx}	1.70×10^5	1.66×10^5	1.74×10^5	1.37×10^5	1.44×10^5	1.49×10^5
γ_{yyyy}	9.67×10^5	1.30×10^6	1.80×10^6	6.40×10^5	8.29×10^5	9.50×10^5
γ_{zzzz}	3.68×10^5	4.29×10^5	2.57×10^5	3.58×10^5	5.49×10^5	2.82×10^5
γ_X	6.84×10^4	6.76×10^4	6.53×10^4	6.03×10^4	6.98×10^4	2.98×10^5
γ_Y	2.37×10^5	2.66×10^5	4.03×10^5	1.74×10^5	2.32×10^5	6.76×10^4
γ_Z	1.09×10^5	1.19×10^5	9.32×10^4	1.08×10^5	1.60×10^5	1.19×10^5
$\gamma_{\rm tot}$	4.16×10^5	4.82×10^5	5.62×10^5	3.43×10^5	4.63×10^5	4.52×10^5
$\gamma_{yyyy}^{\rm FF}$	9.69×10^5	1.30×10^6	1.81×10^6	6.57×10^5	8.46×10^5	9.69×10^5

measured *via* the *Z*-scan, is 12.23×10^{-13} esu.[45] The γ value calculated at the CAM-B3LYP/6-311++G(d,p) level in DMSO is -33.93×10^{-36} esu. The γ_{tot} values for BOD-based systems (1.73×10^{-34}–2.33×10^{-36} esu) are larger than that of Bn-BDY. Thus, these cyclophane-based complexes could be potential excellent NLO molecules.

The unit sphere representation (USR) method[46] of hyperpolarizability can intuitively characterize the molecular response properties using hyperpolarizability tensors, serving as a powerful tool for comprehensively representing molecular hyperpolarizability. Fig. 7 presents the USR results for all investigated compounds. The vector representation for γ is depicted by double-sided arrows parallel to the *X*, *Y*, and *Z* axes, where the lengths of the arrows represent the magnitude of γ in each respective direction (γ_X, γ_Y, γ_Z). The molecular plane of all complexes is defined as the *yz*-plane. The analysis shows that the *y*-axis component dominates the overall second hyperpolarizability. This observation is consistent with the computational results in Table 3, which show that γ_{yyyy} exhibits the maximum amplitude among all tensor components, indicating that intramolecular charge transfer primarily occurs along the *y*-axis. For **BDT-BOD**, however, the tensorial component along the *z*-axis is also significant.

In the following discussion, we will only focus on the *y*-component that contributes mostly to the overall hyperpolarizabilities of the molecules. The hyperpolarizability density analysis was performed to further explore the hyperpolarizability results by analyzing the spatial contributions of electrons. The step size exerts a crucial influence on numerical errors in the FF method. To determine a reasonable step size, we initially compared the γ_{yyyy} values of **DN-BOD** calculated through the combined analytical and FF-mixed approach with the results from the FF method. The *y*-component of second hyperpolarizability ($\gamma^{\mathrm{FF}}_{yyyy}$) calculated using step sizes of 0.0005, 0.001, 0.002, and 0.003 a.u. yields values of 9.74×10^5, 9.69×10^5, 1.04×10^6, and 1.18×10^6 a.u., respectively. Among all tested step sizes, 0.001 a.u. yielded the smallest relative error between the γ_{yyyy} (9.50×10^5 a.u.) and $\gamma^{\mathrm{FF}}_{yyyy}$ (9.69×10^5 a.u.), and was therefore adopted for all subsequent calculations in this study. It can be observed that the trend of the $\gamma^{\mathrm{FF}}_{yyyy}$ values is consistent with that of the γ_{yyyy} values (see Table 3). Fig. 8a presents the integrand functions of the hyperpolarizability densities [$-y\rho^{(3)}_{yyy}(r)$], which illustrates the spatial contribution of electrons to the nonlinear optical (NLO) response. The positive contribution region (yellow) of the $-y\rho^{(3)}_{yyy}(r)$ function is overwhelmingly larger than the negative part (purple) in every molecule, leading to their positive *y*-component of second hyperpolarizability (γ_{yyyy}). The molecules with NDI as the acceptor unit exhibit significantly larger regions of positive contribution compared to the corresponding molecules with BOD as the acceptor.

We further analyze the quantitative contribution of various molecular units to the *y*-components of second hyperpolarizability by employing the multicenter numerical integration algorithm.[47] These molecules are divided into three fragments: the KZ/BDT/DN fragment, the NDI/BOD fragment, and the covalent linkers (–C_6H_4–CH_2–). The decomposition of the hyperpolarizability contribution is summarized in Table S5 (ESI†) and Fig. 8b. For NDI-based systems, the contribution of donors increases significantly from KZ (15.9%) to DN (30.0%), while the contribution from the NDI acceptors gradually decreases (24.1%, 16.4%, and 12.3%). For the BOD-based system, the donor contribution is in the order of

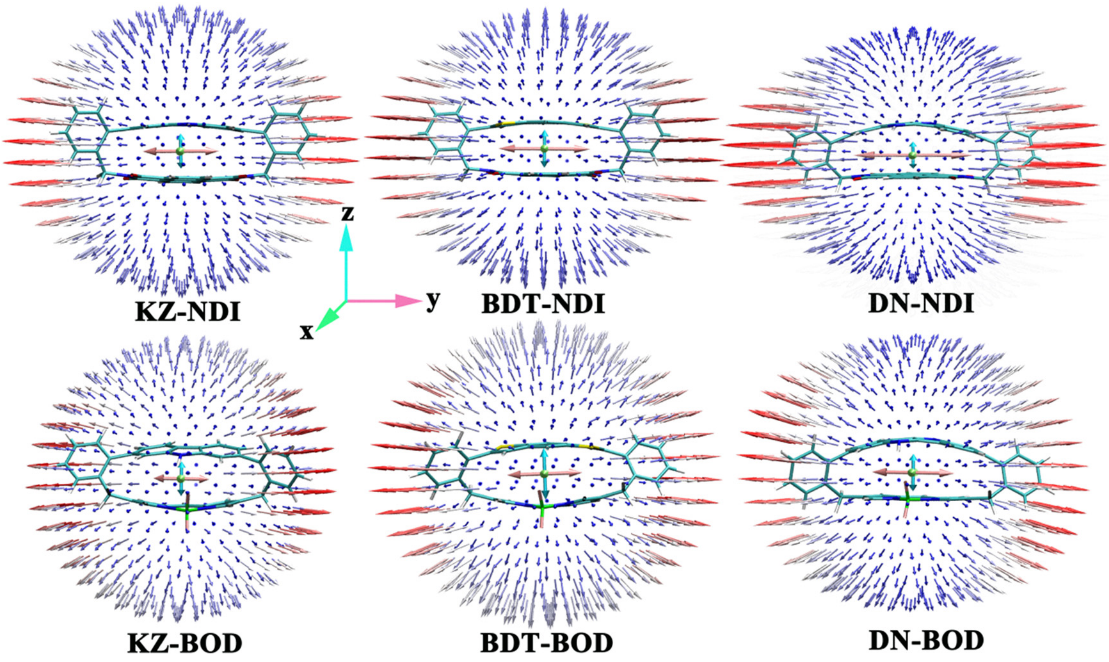

Fig. 7 Unit sphere representation of the second hperpolarizability tensor. The multiplication factor is 0.00001 for the γ vector and 0.000003 for the USR.

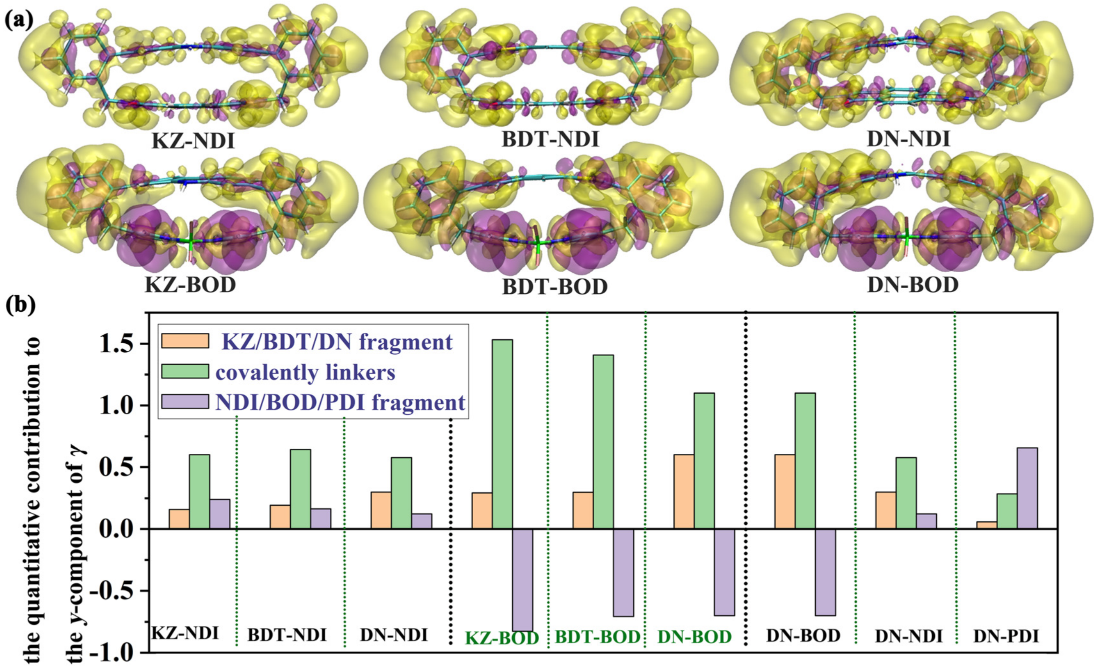

Fig. 8 (a) Plots of $-y\rho^{(3)}_{yyy}(r)$ for the complexes, where yellow and purple isosurfaces represent the positive and negative contributions to γ_{yyyy} values. The isosurfaces are set to 400.0 a.u. (b) Decomposition of the y-component of second hyperpolarizability of the studied into three partial contributions.

DN (60.0%) > BDT (29.8%) > KZ (29.3%), and the BOD acceptor exhibits a substantial negative contribution (−70.0% to −82.6%), suggesting the presence of a charge transfer offset effect. The progressive increase in the donor contribution from KZ to DN correlates with their electron-donating strengths. Additionally, we calculated the second hyperpolarizability of **DN-PDI** (see Fig. S2, ESI†). Perylenediimide (PDI) exhibits superior electron-accepting capability compared to naphthalenediimide (NDI), as demonstrated by its significantly higher electron affinity (EA) [2.12 eV (PDI) > 1.84 eV (NDI) at the CAM-B3LYP/6-31G(d,p)]. The γ_{tot} value of **DN-PDI** is 1.59×10^6 a.u., which is higher than **DN-NDI**. The plot of $-y\rho^{(3)}_{yyy}(r)$ together with the corresponding $\gamma^{\text{FF}}_{yyyy}$ value (6.19×10^6 a.u.) of the **DN-PDI** is provided in Fig. S2 (ESI†). We compared the fragment contributions of the **DN-BOD**, **DN-NDI**, and **DN-PDI** molecules. The order of electron acceptor contribution is BOD (−70.0%) < NDI (12.3%) < PDI (65.6%), demonstrating that enhanced acceptor strength typically augments positive contributions—except for the BOD's anomalous negative effect attributed to its weak electron-accepting character.

To interpret the variation of the second hyperpolarizability of the studied systems, the simplified two-level model derived from the sum-over-state (SOS) approach was employed. The two-level model can be expressed as follows: $\gamma \propto f_{\text{os}}{}^2/\Delta E_{\text{ge}}{}^5$, where f_{os} corresponds to the oscillator strength and ΔE_{ge} denotes the transition energy. The ΔE_{ge}, f_{os}, and $f_{\text{os}}{}^2/\Delta E_{\text{ge}}{}^5$ values are presented in Table 2. According to the two-level expression, the γ value is proportional to the quadratic power of f_{os} but inversely proportional to the fifth power of ΔE_{ge}. For the NDI-based systems, the $f_{\text{os}}{}^2/\Delta E_{\text{ge}}{}^5$ values were determined as 2083 a.u. (**KZ-NDI**, S3 state), 1916 a.u. (**BDT-NDI**, S3 state), and

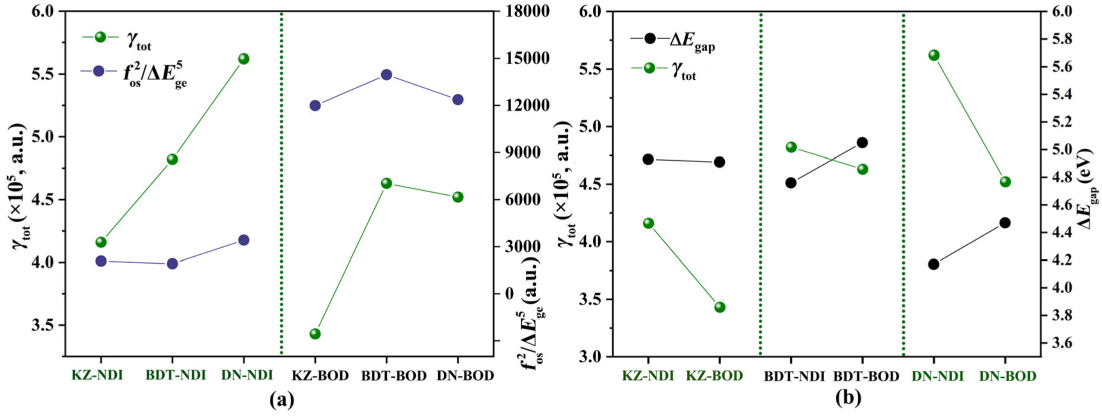

Fig. 9 (a) The relationship between γ_{tot} and $f_{\text{os}}{}^2/\Delta E_{\text{ge}}{}^5$ values for the studied complexes. (b) The relationship between γ_{tot} and ΔE_{gap} values.

3413 a.u. (**DN-NDI**, S7 state), while the BOD-based systems showed significantly higher values of 11 988 a.u. (**KZ-BOD**, S1 state), 13 957 a.u. (**BDT-BOD**, S1 state), and 12 367 a.u. (**DN-BOD**, S2 state). Fig. 9a shows that the estimated $f_{\rm os}{}^2/\Delta E_{\rm ge}{}^5$ values follow essentially the same trend as exactly calculated $\gamma_{\rm tot}$ values. Therefore, for the NDI-based systems, the presence of multiple significant excited states cannot be overlooked. Generally, molecules exhibiting lower transition energies tend to yield larger second hyperpolarizabilities, as exemplified by **KZ-NDI**, **BDT-NDI**, **KZ-BOD**, **BDT-BOD**, and **DN-BOD**. In these systems, the excited state with the smallest $\Delta E_{\rm ge}$ corresponds to the maximum γ value, underscoring $\Delta E_{\rm ge}$ as the predominant factor governing the second hyperpolarizability. However, exceptions arise in **DN-NDI**, where the excited state with a higher $\Delta E_{\rm ge}$ and a larger $f_{\rm os}$ yields the maximum value of $f_{\rm os}{}^2/\Delta E_{\rm ge}{}^5$. This highlights the dual influence of both $\Delta E_{\rm ge}$ and $f_{\rm os}$ on the nonlinear optical response. These results demonstrate that the nonlinear optical (NLO) response magnitudes can be systematically tuned through strategic donor–acceptor co-assembly, thereby enabling precise control over optoelectronic properties. Furthermore, Fig. 9b plots the correlation between $\Delta E_{\rm gap}$ and $\gamma_{\rm tot}$. Notably, NDI-based molecules with small energy gaps demonstrate superior $\gamma_{\rm tot}$ values relative to BOD analogues, excluding **KZ-NDI** and **KZ-BOD**.

4. Conclusions

In this study, we systematically investigated the geometric structures, electronic properties, and nonlinear optical responses of a series of cyclophane-based donor–acceptor complexes using density functional theory calculations. Reduced density gradient analysis confirms weak π–π interactions between donor (KZ/BDT/DN) and acceptor (NDI/BOD) units, while charge analysis (NPA and ADCH) and electrostatic potential maps highlight charge transfer characteristics. All complexes displayed exceptionally large second hyperpolarizabilities ($\gamma_{\rm tot}$), ranging from 3.43×10^5 to 5.62×10^5 a.u. Notably, NDI-based systems exhibit larger second hyperpolarizabilities than BOD-based analogs. Hyperpolarizability density analysis revealed that donor contributions scaled with electron-donating ability (KZ < BDT < DN), while acceptor contributions followed the trend PDI > NDI > BOD (with BOD exhibiting anomalous negative contributions). The two-level model underscores that lower transition energies and higher oscillator strengths synergistically enhance $\gamma_{\rm tot}$ values. This study provides valuable theoretical guidance and experimental references for the development of novel NLO materials.

Conflicts of interest

There are no conflicts to declare.

Data availability

The data supporting this article have been included as part of the ESI.†

References

1 P. Chen, C. Wang, D. Wei, Y. Hu, X. Xu, J. Li, D. Wu, J. Ma, S. Ji, L. Zhang, L. Xu, T. Wang, C. Xu, J. Chu, S. Zhu, M. Xiao and Y. Zhang, *Light: Sci. Appl.*, 2021, **10**, 146.

2 A. Autere, H. Jussila, Y. Dai, Y. Wang, H. Lipsanen and Z. Sun, *Adv. Mater.*, 2018, **30**, 1705963.

3 M. Klikar, P. le Poul, A. Růžička, O. Pytela, A. Barsella, K. D. Dorkenoo, F. Robin-le Guen, F. Bureš and S. Achelle, *J. Org. Chem.*, 2017, **82**, 9435–9451.

4 Z. Liu, F. Gan, N. Dong, B. Zhang, J. Wang and Y. Chen, *J. Mater. Chem.*, 2019, **7**, 10789–10794.

5 I. D. L. Albert, T. J. Marks and M. A. Ratner, *J. Am. Chem. Soc.*, 1997, **119**, 6575–6582.

6 E. Rtibi, M. Abderrabba, S. Ayadi and B. Champagne, *Inorg. Chem.*, 2019, **58**, 11210–11219.

7 J. Li, W. Chen, J. Liu, W. Sun, Z. Li and Y. Li, *Dalton Trans.*, 2021, **50**, 4613–4622.

8 B. Abdelaziz, Z. Mazouz, B. Gassoumi, N. E. I. Boukortt, S. Patanè and S. Ayachi, *J. Mol. Liq.*, 2024, **395**, 123934.

9 Y. Yao, H. L. Xu and Z. M. Su, *J. Mater. Chem. C*, 2022, **10**, 12338.

10 S. Kumar, J. Shukla, Y. Kumar and P. Mukhopadhyay, *Org. Chem. Front.*, 2018, **5**, 2254–2276.

11 L. Wang, Y. L. Liu, Q. J. Li, S. H. Chen, D. He and M. S. Wang, *J. Phys. Chem. A*, 2022, **126**, 870–878.

12 L. Wang, Y. L. Liu and M. S. Wang, *Phys. Chem. Chem. Phys.*, 2022, **24**, 29747–29756.

13 L. Wang, Y. L. Liu and M. S. Wang, *Langmuir*, 2023, **39**, 357–366.

14 S. Tongsuk, R. Malatong, T. Unjarern, C. Wongkaew, P. Surawatanawong, T. Sudyoadsuk, V. Promarak and N. Ruangsupapichat, *J. Lumin.*, 2021, **238**, 118287.

15 Y. Wei, Q. Peng, C. Zhong, S. Ma, T. Wang, Y. Pu, W. Zhang, S. Wang and L. Xie, *Dyes Pigm.*, 2024, **225**, 112097.

16 S. Bhattacharya, C. Biswas, S. S. K. Raavi, J. Venkata Suman Krishna, N. Vamsi Krishna, L. Giribabu and V. R. Soma, *J. Phys. Chem. C*, 2019, **123**, 11118–11133.

17 M. Rajeshirke, M. C. Sreenath, S. Chitrambalam, I. H. Joe and N. Sekar, *J. Phys. Chem. C*, 2018, **122**, 14313–14325.

18 P. Si, J. Liu, Z. Zhen, X. Liu, G. Lakshminarayana and I. V. Kityk, *Tetrahedron Lett.*, 2012, **53**, 3393–3396.

19 I. Roy, A. H. G. David, P. J. Das, D. J. Pe and J. F. Stoddart, *Chem. Soc. Rev.*, 2022, **51**, 5557–5605.

20 S. Gabutti, S. Schaffner, M. Neuburger, M. Fischer, G. Schäfer and M. Mayor, *Org. Biomol. Chem.*, 2009, **7**, 3222–3229.

21 D. Bansal, A. Kundu, V. P. Singh, A. K. Pal, A. Datta, J. Dasgupta and P. Mukhopadhyay, *Chem. Sci.*, 2022, **13**, 11506–11512.

22 Z. Wang, Y. Liu, X. Quan, W. Zhang, R. Tan, H. Gu, C. Sheng, C. Duan, P. Xing and J.-H. Wan, *Angew. Chem., Int. Ed.*, 2024, **64**, e202413295.

23 V. K. Shukla, S. S. Sonavane and N. Sekar, *Spectrochim. Acta, Part A*, 2024, **321**, 124674.

24 H. B. Gobeze, S. Kumar, F. D'Souza and M. Ravikanth, *Chem. – Eur. J.*, 2017, **23**, 1546–1556.

25 X. Lin, D. Tang, T. He, Z. Xu, H. Qiu, Q. Zhang and S. Yin, *Spectrochim. Acta, Part A*, 2019, **217**, 164–169.

26 H. Kang, J. Ye, H. Wang, Y. Zhang and Y. Qiu, *Theor. Chem. Acc.*, 2021, **140**, 47.

27 H. Q. Wang, J. T. Ye, Y. Zhang, Y. Y. Zhao and Y. Q. Qiu, *J. Mater. Chem. C*, 2019, **7**, 7531–7547.

28 R. Mallah, M. C. Sreenath, S. Chitrambalam, I. H. Joe and N. Sekar, *Opt. Mater.*, 2018, **84**, 795–806.

29 C. L. Qu, Z. M. Su and F. W. Gao, *New J. Chem.*, 2021, **45**, 4335–4339.

30 M. J. Frisch, G. W. Trucks, H. B. Schlegel, G. E. Scuseria, M. A. Robb, J. R. Cheeseman, G. Scalmani, V. Barone, B. Mennucci, G. A. Petersson, H. Nakatsuji, M. Caricato, X. Li, H. P. Hratchian, A. F. Izmaylov, J. Bloino, G. Zheng, J. L. Sonnenberg, M. Hada, M. Ehara, K. Toyota, R. Fukuda, J. Hasegawa, M. Ishida, T. Nakajima, Y. Honda, O. Kitao, H. Nakai, T. Vreven, J. A. Montgomery Jr., J. E. Peralta, F. Ogliaro, M. earpark, J. J. Heyd, E. Brothers, K. N. Kudin, V. N. Staroverov, R. Kobayashi, J. Normand, K. Raghavachari, A. Rendell, J. C. Burant, B. Cross, V. Bakken, C. Adamo, J. Jaramillo, R. Gomperts, R. E. Stratmann, O. Yazyev, A. J. Austin, R. Cammi, C. Pomelli, J. W. Ochterski, R. L. Martin, K. Morokuma, V. G. Zakrzewski, G. A. Voth, P. Salvador, J. J. Dannenberg, S. Dapprich, A. D. Daniels, O. Farkas, J. B. Foresman, J. V. Ortiz, J. Cioslowski and D. J. Fox, *Gaussian 09, Revision E.01*, Gaussian, Inc., Wallingford, CT, 2013.

31 T. Lu and F. W. Chen, *J. Comput. Chem.*, 2012, **33**, 580–592.

32 W. Humphrey, A. Dalke and K. Schulten, *J. Mol. Graphics*, 1996, **14**, 33–38.

33 Y. Zhao and D. G. Truhlar, *Theor. Chem. Acc.*, 2008, **120**, 215–241.

34 T. Yanai, D. P. Tew and N. C. Handy, *Chem. Phys. Lett.*, 2004, **393**, 51–57.

35 L. Goerigk and S. Grimme, *Phys. Chem. Chem. Phys.*, 2011, **13**, 6670–6688.

36 S. Tsuzuki and T. Uchimaru, *Phys. Chem. Chem. Phys.*, 2020, **20**, 22508–22519.

37 A. E. Reed, R. B. Weinstock and F. Weinhold, *J. Chem. Phys.*, 1985, **83**, 735–746.

38 L. U. Tian and F. Chen, *J. Comput. Theor. Chem.*, 2012, **11**, 163–183.

39 Z. Liu, T. Lu and Q. Chen, *Carbon*, 2020, **165**, 461–467.

40 V. Barone, M. Cossi and J. Tomasi, *J. Chem. Phys.*, 1997, **107**, 3210–3221.

41 A. Loudet and K. Burgess, *Chem. Rev.*, 2007, **107**, 4891–4932.

42 R. R. Mallah, D. R. Mohbiya, M. C. Sreenath, S. Chitrambalam, I. H. Joe and N. Sekar, *Spectrochim. Acta, Part A*, 2019, **209**, 126–140.

43 E. R. Johnson, S. Keinan, P. Mori-Sánchez, J. Contreras-García, A. J. Cohen and W. Yang, *J. Am. Chem. Soc.*, 2010, **132**, 6498–6506.

44 H. P. Li, X. P. Shen, K. Han, G. Tang and Z. H. Zhang, *Comput. Theor. Chem.*, 2013, **1023**, 95–98.

45 L. Wu and K. Burgess, *Chem. Commun.*, 2008, 4933–4935.

46 A. E. Tuer, S. Krouglov, N. Prent, R. Cisek, D. Sandkuijl, K. Yasufuku, B. C. Wilson and V. Barzda, *J. Phys. Chem. B*, 2011, **115**, 12759–12769.

47 A. D. Becke, *J. Chem. Phys.*, 1988, **88**, 2547–2553.